ACS APPLIED MATERIALS & INTERFACES

Spotlight on Applications

www.acsami.org

The Heat-Transfer Method: A Versatile Low-Cost, Label-Free, Fast, and User-Friendly Readout Platform for Biosensor Applications

Bart van Grinsven,*[,†,‡,⊥] Kasper Eersels,[‡] Marloes Peeters,[‡] Patricia Losada-Pérez,[‡] Thijs Vandenryt,[‡] Thomas J. Cleij,[†] and Patrick Wagner[‡,§]

[†]Maastricht Science Programme, Maastricht University, PO Box 616, 6200 MD Maastricht, The Netherlands

[‡]Institute for Materials Research IMO and [§]IMEC vzw, IMOMEC Division, Hasselt University, Wetenschapspark 1, B3590 Diepenbeek, Belgium

ABSTRACT: In recent years, biosensors have become increasingly important in various scientific domains including medicine, biology, and pharmacology, resulting in an increased demand for fast and effective readout techniques. In this Spotlight on Applications, we report on the recently developed heat-transfer method (HTM) and illustrate the use of the technique by zooming in on four established bio(mimetic) sensor applications: (i) mutation analysis in DNA sequences, (ii) cancer cell identification through surface-imprinted polymers, (iii) detection of neurotransmitters with molecularly imprinted polymers, and (iv) phase-transition analysis in lipid vesicle layers. The methodology is based on changes in heat-transfer resistance at a functionalized solid−liquid interface. To this extent, the device applies a temperature gradient over this interface and monitors the temperature underneath and above the functionalized chip in time. The heat-transfer resistance can be obtained by dividing this temperature gradient by the power needed to achieve a programmed temperature. The low-cost, fast, label-free and user-friendly nature of the technology in combination with a high degree of specificity, selectivity, and sensitivity makes HTM a promising sensor technology.

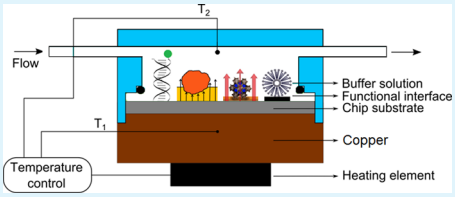

KEYWORDS: *biosensors, heat-transfer method, DNA, cancer cells, neurotransmitters, lipid vesicles*

1. INTRODUCTION

In this Spotlight on Applications, we evaluate the recently developed heat-transfer method (HTM) as a versatile biosensor readout platform. The methodology can be combined with a wide range of functional interfaces, leading to the development of numerous applications. One of the major demands when developing a diagnostic application is the label-free, low-cost, fast, sensitive, and user-friendly nature of the proposed technology. To meet these requirements, research in the field of biosensors has become increasingly important in recent years.

Biosensors have evolved from a canary in a coal mine to more complex, technological devices for a vast number of applications in areas as diverse as, for example, (bio)medical research, environmental analysis, or pharmacology.[1] Generally speaking, a biosensor can be defined as an analytical device that combines a biological receptor element with a physicochemical detector.[2] Biosensor platforms profit from the high degree of specificity that a natural receptor has for its target to detect the analyte of interest. This natural receptor layer can consist of nucleic acids (DNA or RNA),[3−5] enzymes,[6−8] cells,[9−11] or antibodies.[12,13]

Biosensors based on biological recognition elements can be very sensitive and specific toward their target, but there are drawbacks associated with the use of biological receptors. They can be unstable in challenging physical and chemical environments, display a limited shelf life, it is time-consuming and expensive to obtain these receptors in sufficiently large quantities, and some analytes do not have a natural receptor.[14] Many of these drawbacks can be overcome by using synthetic rather than natural receptors in so-called biomimetic sensors. Molecularly imprinted polymers (MIPs)[15−17] and surface-imprinted polymers (SIPs)[18] are often used as synthetic receptors in these devices.

Bio(mimetic)sensor platforms can be combined with several readout techniques to detect target binding to the functional interface. These detection methods are often based on electrochemical detection methods including impedance spectroscopy,[19,20] cyclic voltammetry,[21,22] field-effect,[23,24] potentiometry,[25,26] amperometry,[27,28] etc. Alternatively, biosensor applications have been developed based on optical,[29,30] microgravimetrical,[31,32] and thermal[33] detection. The underlying principles of these sensing techniques are associated with several phenomena occurring at a solid−liquid interface including: target-receptor binding, changes in the total charge, mass, refractive index or dielectric constant at the interface, change in mechanical rigidity, or redistribution of counter-ions.[34−39]

In this article, we review the use of a new readout technology based on thermal transport through a functionalized solid−liquid interface, the heat-transfer method. This method surfaced in 2012 and was originally used for the detection of single-

Received: June 10, 2014
Accepted: August 8, 2014
Published: August 8, 2014

nucleotide polymorphisms (SNPs) in DNA.[40] However, the technique has proven to be very versatile, and the application can vary based on the type of functional interface used, including specific cell detection,[41] small organic molecule detection,[42] and phase transition analysis in lipid vesicle layers.[43]

2. GENERAL HEAT TRANSFER METHOD CONCEPT

The concept of HTM is based on the analysis of thermal transport through functional interfaces. Specific changes at the solid−liquid interface can lead to a change in thermal resistance (R_{th}). Without being exhaustive, these changes include DNA hybridization/denaturation, target-receptor binding, and phase transitions in lipid vesicles. These effects are described in detail in the Applications.

The HTM setup is illustrated in Figure 1. The central element through which the heat flux will pass consists of a chip serving as an immobilization platform onto which the functional interface is applied. This chip is pressed mechanically with its backside onto a polished copper block which serves as heat provider or heat sink. The internal temperature of the copper block, T_1, is measured by a thermocouple and steered via a proportional-integral-derivative controller (PID controller), connected to a power resistor. Possible heat-transfer losses between copper and silicon are minimized by conductive silver paste. The front side of the functionalized chip is exposed to the medium which contains the target of interest. An O-ring seal defines a contact area of 28 mm^2 between the sensing surface and the liquid. Except for minor heat losses along the seal, heat will mainly be transferred from the chip to the liquid. The temperature in the liquid, T_2, is measured by a second thermocouple, positioned above the solid−liquid interface. To extract the heat-transfer resistance R_{th} (°C/W) quantitatively, the ratio of the temperature difference $\Delta T = T_1 - T_2$ and the input power P according to $R_{th} = \Delta T/P$, is analyzed.[44]

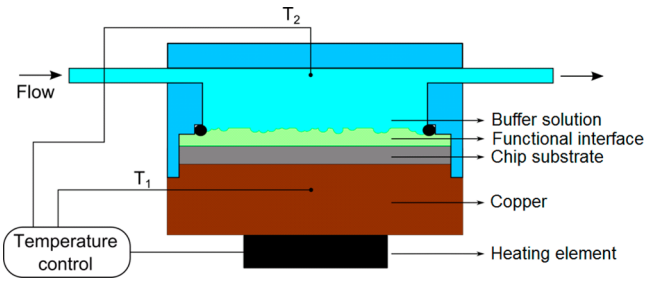

Figure 1. Schematic layout of the HTM setup. The sensor chip is connected to a copper block with the functional interface facing a liquid flow cell. The temperature T_1 of the copper backside contact is measured by a thermocouple and can be actively steered via a controller unit. The temperature T_2 inside the liquid is recorded by using a second thermocouple. The heat-transfer related parameters are the temperature difference $T_1 - T_2$ and the input power P provided by the heating element, allowing the user to monitor the thermal resistance of the solid−liquid interface in time. Reproduced with permission from ref 40. Copyright 2012 American Chemical Society.

3. APPLICATIONS

3.1. SNP Detection in DNA Fragments. The first application developed using HTM as a readout platform involved the detection of SNPs in DNA sequences.[40] The interface through which the thermal transport was analyzed, consisted of a silicon chip coated with a thin layer of boron-doped, nanocrystalline diamond (NCD).[45] This diamond layer served as an immobilization platform that was functionalized by covalently attaching 29-mers of double-stranded(ds)-DNA via the photochemical fatty acid and EDC coupling route.[46] The single-stranded(ss) probe DNA was linked to the diamond surface through stable C−C bonds in head-on configuration, while the target ss-DNA was free to hybridize or to denature according to the experimental conditions without steric hindering, as can be seen in Figure 2a,b. The areal density of probes on the functional interface was in the order of $10^{12} - 10^{13}$ duplexes per cm^2, meaning that the average distance between duplexes is less than the total length of an individual duplex.[47] The effect on the heat-transfer resistance can be

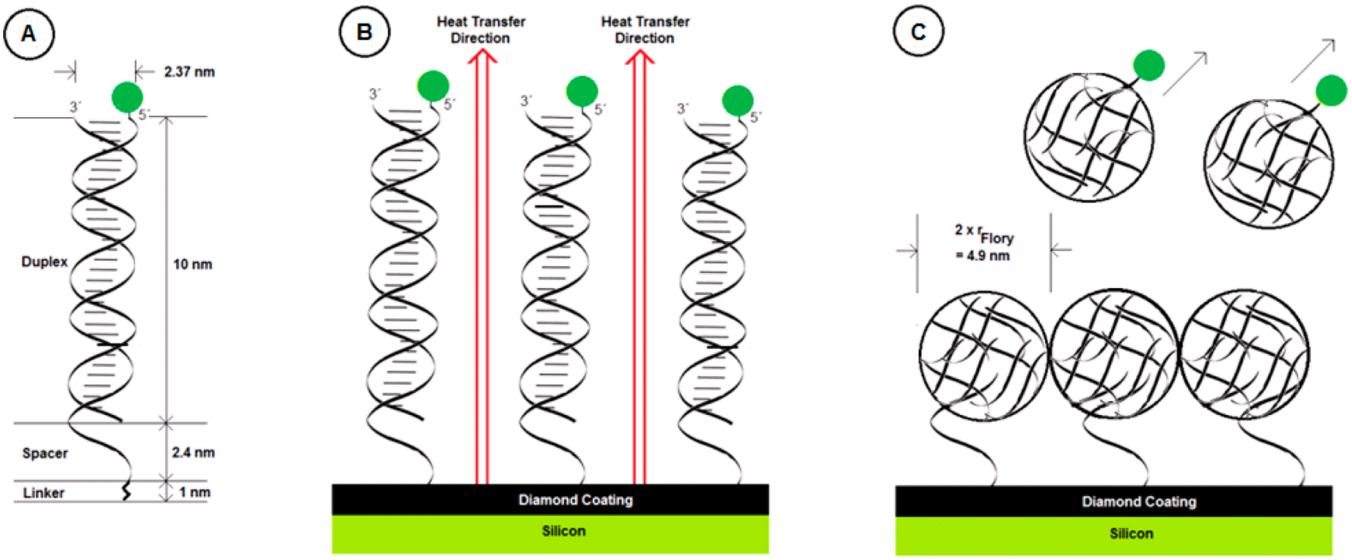

Figure 2. Schematic illustrations. (a) DNA duplexes with labeled targets strand. (b) Heat-transfer path through a molecular DNA brush. (c) Upon denaturation, the probe DNA curls up in irregular structures, characterized by the Flory radius, thereby blocking heat transfer at the solid−liquid interface. Adapted with permission from ref 40. Copyright 2012 American Chemical Society.

explained as follows: the DNA-fragments of 29 base pairs have a length of 10 nm, which is far below the estimated persistence length of 50 nm.[48,49] These ds-DNA fragments can therefore be considered as stiff rods on the functional interface with a tilt angle in the range of 31°−52°.[50,51] Since ds-DNA has a diameter of 2.37 nm, an areal density in the range of 10^{12} − 10^{13} duplexes per cm^2 implies that about 35% of the chip surface was functionalized with ds-DNA. The remaining 65% still consisted of nonfunctionalized NCD, as can be seen from the schematic illustration in Figure 2b. Thermal energy is transferred from the phonons in the diamond lattice to the water molecules partially through the unaltered surface. However, some of the heat dissipates along ds-DNA based on molecular vibrations.[44] Denaturation is induced by increasing the temperature T_1 from 35.0 to 85.0 °C. After denaturation of the ds-DNA, the remaining probe DNA fragments have a total length of 36 base pairs (L = 12.24 nm). Since the persistence length of ss-DNA is only 1.48 nm,[48] the ss-DNA fragments will curl up in irregular shapes with a Flory radius of 2.46 nm. This will result in a nominal increase of the surface coverage to 150%, leading to a higher thermal resistance of the functional interface (Figure 2c).

The effect of denaturing ds-DNA on thermal conduction was used for the detection of SNPs in DNA. The results of this experiment are summarized in Figure 3. Exposing a nonfunctionalized diamond chip to an aqueous solution resulted in a stable and widely temperature-independent R_{th} value of about 6.7 − 7.0 °C/W (red line). Attachment of the fatty-acid cross-linker did not result in a measurable increase in R_{th} (purple line), which can be explained by the fact that the diameter of this dense layer of alkyl chains is only 1 nm. The R_{th} increases to 9.0 °C/W at 40.0 °C upon attachment of probe ss-DNA fragments and decreases monotonously to 8.4 °C/W at 80.0 °C (blue line). This sample was hybridized with complementary DNA (black line) as well as DNA containing a CC-mismatch at base pair 7 (green line) and base pair 20 (orange line). All of these curves clearly exhibit a stepwise increase in R_{th} upon denaturation of the ds-DNA. The midpoint of each temperature curve: 63.0 ± 0.1 °C (black line), 57.6 ± 0.1 °C (green line), and 56.8 ± 0.1 °C (orange line) can be used to discriminate between complementary DNA fragments and fragments containing a SNP. The presence of a SNP in the target fragment leads to a decreased stability of the resulting DNA-duplex, measured as a decrease in melting temperature.

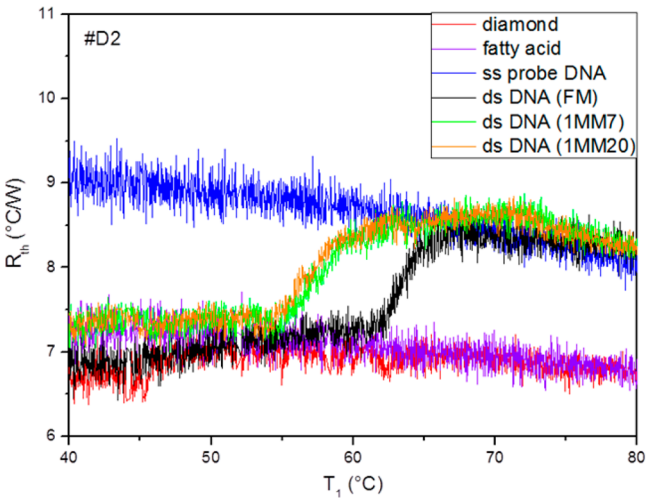

Figure 3. Heat-transfer resistance R_{th} as a function of temperature (data have not been filtered). The unmodified electrode (red line) and the electrode with covalently attached fatty-acid linkers (purple line) have a widely temperature independent R_{th} around 7.0 °C/W. In the configuration with attached probe DNA (blue line) the heat-transfer resistance has notably increased to 9.0 °C/W, indicating an efficient thermal insulation by the highly flexible ss-DNA fragments. The R_{th} of double-stranded DNA (black line for the complementary duplexes) is comparable to the nonmodified surface at low temperatures and switches to the ss-DNA behavior upon denaturation with a midpoint temperature $T_{midpoint}$ = 63.0 °C ± 0.1 °C. Repeating the experiment with defective DNA duplexes results in a clear shift of $T_{midpoint}$ to lower temperatures: for the duplex with CC-mismatch at BP 7 (green line) we obtain $T_{midpoint}$ = 57.6 °C ± 0.1 °C and for the same mismatch at BP 20 (orange line) this is 56.8 °C ± 0.1 °C. Adapted with permission from ref 40. Copyright 2012 American Chemical Society.

Elaborating on the possibility of determining the melting temperature of a DNA sequence by means of HTM, it was shown in 2013 that the heat transfer resistivity procedure allows for differentiation between DNA fragments representing different sequence polymorphisms of the same gene when analyzed simultaneously. This illustrated the potential of this technique as a user-friendly alternative for currently widely used microarrays.[52] Moreover, the procedure allowed to estimate the mutated fraction of the gene of interest through simultaneous heat transfer resistance analysis of both sequence polymorphisms.[53] All this information led to the decision that the HTM technology should be tested in a clinical environment. In this study the technology was evaluated as an alternative method to detect phenylketonuria (PKU)-related mutations in a label-free, real-time manner in patient samples.[54] The experiments on DNA present HTM as a technique with great potential for implementation in diagnostic procedures in any field of research ranging from clinical diagnostics, environmental microbiology, and microbial ecology to detect mutations or polymorphisms.

3.2. Specific Cell Detection. The combination of HTM with so-called surface imprinted polymers, has demonstrated the potential of the methodology for biomedical applications based on specific cell detection.[41] Functional interfaces were created by coating aluminum chips (10 × 10 mm^2) with semicured polyurethane. Cell-covered polydimethysiloxane (PDMS) stamps were gently pressed into this polymer layer. Upon curing of the layer, the stamp was removed, resulting in a pattern of microcavities on the surface of the polymer. The functional and morphological complementarity between these cavities and the template cells makes it possible for cells to rebind to their receptor in a selective and specific manner.[55]

The detection principle is shown in Figure 4. The thermal resistance of an empty SIP is determined by the thickness of the polyurethane layer, indicating that the R_{th} of the microcavities is lower in comparison to the thicker nonimprinted areas of the SIP. These microcavities will therefore act as preferential heat-channels (Figure 4a). Rebinding of cells into these cavities will result in an increase in R_{th} at the solid−liquid interface as it was recently shown that phospholipid bilayers have a higher thermal resistance than water (Figure 4b).[56]

This effect was used for the specific detection of cancer cells in buffer solution.[41] The setup was used to discriminate between breast-cancer cells (MCF-7 cells) and immortalized T-lymphocytes, associated with leukemia (Jurkat cells). In addition, it was analyzed if the methodology could discriminate between these cancer cells and a mixed population of healthy blood cells (peripheral blood mononuclear cells or PBMCs).

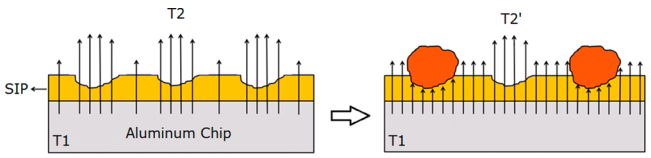

Figure 4. Concept of heat transfer through surface-imprinted polyurethane layers. The arrows indicate the heat-transfer direction. (a) The thermal resistance of an empty SIP is determined by the thickness of the polyurethane layer. Therefore, most of the heat will dissipate through the microcavities. (b) Cell binding blocks the heat transfer through the imprints, causing the thermal resistance at the solid–liquid interface to increase. Adapted with permission from ref 41. Copyright 2013 American Chemical Society.

Exposing a SIP imprinted for the MCF-7 cells to a solution of target cells in PBS, led to an increase in thermal resistance from 6.09 ± 0.2 to 7.05 ± 0.1 °C/W (Figure 5a, black line). There appears to be some moderate degree of cross-selectivity when Jurkat cells bind to MCF-7 imprints, leading to an increase in R_{th} from 6.02 ± 0.1 to 6.35 ± 0.1 °C/W (red line). The signal returns back to baseline upon flushing the flow cell with phosphate-buffered saline (PBS) at flow rates of 0.25 and 2.5 mL/min. This indicates that the mechanical friction provided by flushing the flow cell with buffer is sufficiently strong to remove the nonspecifically bound competitor cells from the binding cavities. However, the shear forces are not strong enough to remove the target cells from the SIP, as evidenced by the observation that the black line remains at an elevated R_{th} level after both washing steps. Exposing the MCF-7 SIP to healthy peripheral blood mononuclear cells (PBMC's) did not result in a measurable increase in thermal resistance (blue line).

To construct a full cross-selectivity matrix, the experiment was repeated with Jurkat (Figure 5b) and PBMC (Figure 5c) SIPs. Minor but measurable cross-selectivity effects are observed resulting from (i) MCF-7 cells and PBMC's binding to Jurkat SIPs (black and blue line in Figure 5b) and (ii) Jurkat cells binding to PBMC SIPs (red line in Figure 5c). In all cases,

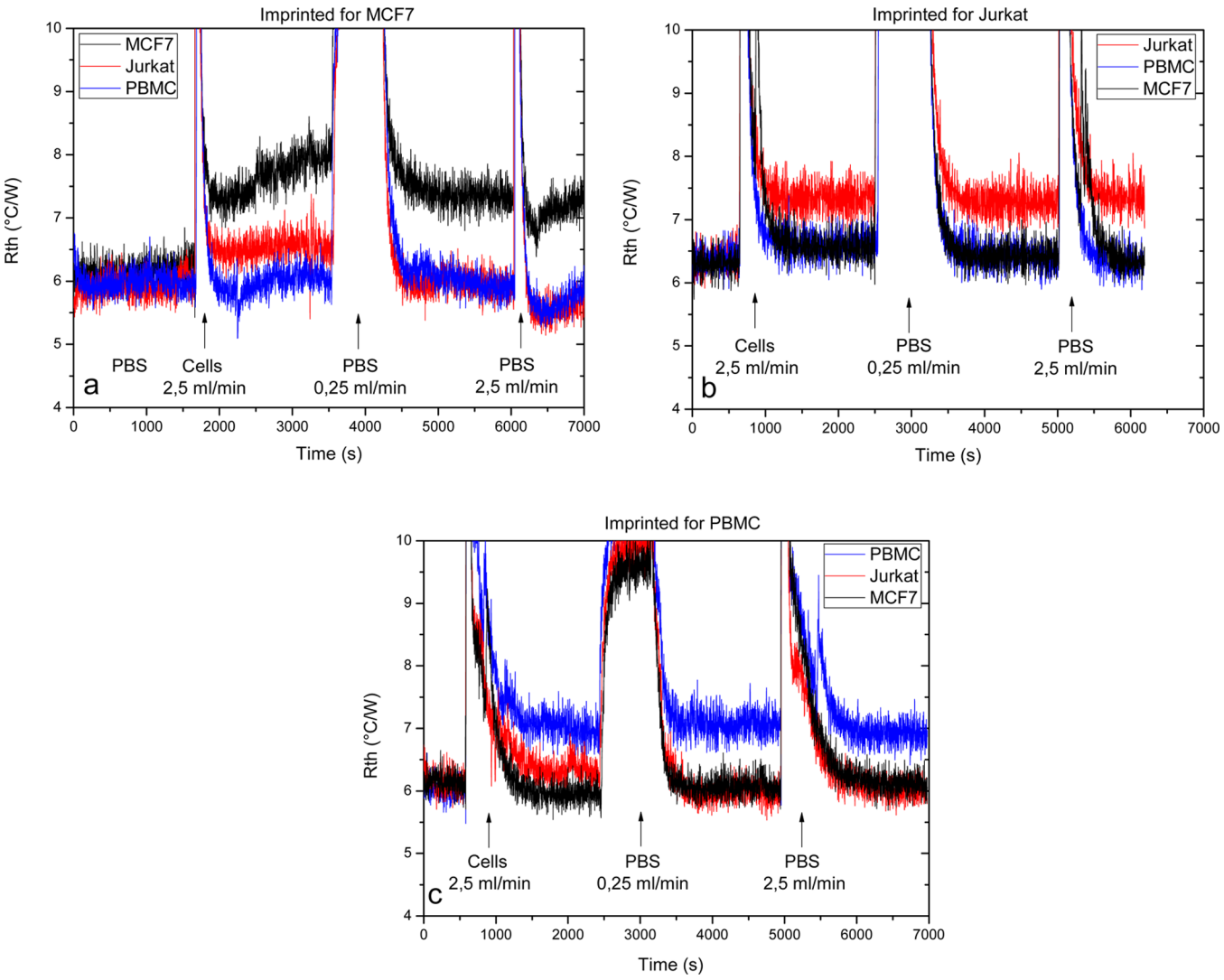

Figure 5. Heat-transfer resistance as a function of time shown for: (a) MCF-7 imprinted SIP toward MCF-7 cells (black line), Jurkat cells (red line), and PBMC (blue line). (b) Jurkat-imprinted SIP toward Jurkat-, PBMC-, and MCF-7 cells with consecutive rinsing; the color code is identical with (a). (c) Thermal response of a PBMC-imprinted SIP toward PBMC-, Jurkat-, and MCF-7 cells. The color code and rinsing steps are identical with (a, b). Mild rinsing with cell-free PBS brings the cross-selective response for nontarget cells back to baseline in (a, b, and c). Adapted with permission from ref 41. Copyright 2013 American Chemical Society.

the nonspecific binding of competitor cells to the SIP can be reversed by flushing the layer with buffer solution.

The experiment described above illustrates that the combination of HTM with SIPs results in a biomimetic sensor platform that could lead to the development of diagnostic applications for the specific detection of circulating tumor cells (CTCs). State-of-the-art CTC detection platforms are usually based on fluorescence-activated cell sorting (FACS), a specialized type of flow cytometry. Although this technique is very sensitive, it requires expensive instrumentation and fluorescent labeling, and it must be operated by medically trained personnel in a lab environment.[57] HTM can offer a low-cost, user-friendly and label-free alternative that can be used on the bench. However, to detect CTCs in patient samples, the sensitivity of the device needs to be increased. Therefore, the proposed detection limit, being in the range of 10^4 cells/ml, needs to be improved. In 2014 it was shown that the sensitivity of the methodology can be boosted by using a progressive enrichment approach. SIP layers were exposed to mixed cell solutions in multiple consecutive exposure runs, making it possible to detect target cells in the presence of competitor cells differing only in the expression of a single protein, at a ratio of 1:100.[58]

3.3. Specific Detection of Small Organic Molecules.

Recent work has shown that it is possible to use HTM for the detection of small organic molecules using molecularly imprinted polymers (MIPs) as synthetic receptors.[42] To construct the sensor platform, first MIP particles are obtained by bulk polymerization as described in more detail in previous studies.[20] Functional interfaces are created by pressing a MIP-covered PDMS stamp onto an aluminum chip coated with an adhesive layer. Upon exposure of the MIP-functionalized substrate to its original template, an increase in the thermal resistance is observed. This can be explained qualitatively by the pore-blocking model, which is schematically shown in Figure 6.

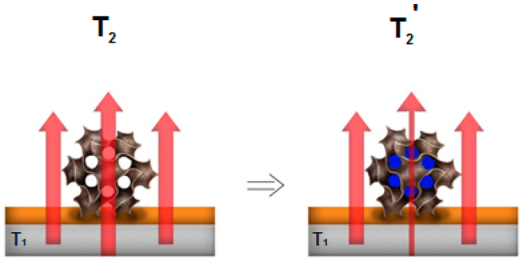

Figure 6. Artist's impression of the pore-blocking model. The MIP particle, embedded in the surface, contains various pores where binding sites are present for its template. When these channels are filled by target molecules (indicated by blue dots), heat flux through the MIP layer is strongly reduced. As a result, the temperature in the fluid (T_2) will be lowered. Adapted with permission from ref 42. Copyright 2014 Springer.

Upon rebinding, the heat flux through one cavity is strongly reduced due to the presence of the template (Figure 6). As a result, theoretically speaking, the total heat-transfer resistance will be increased. The more of the target will be bound, the more cavities will exhibit this behavior leading to an ultimately higher effect size. For proof-of-principle purposes, aluminum electrodes were functionalized with MIP particles for L-nicotine and measurements were performed in PBS solutions.[42] The dose–response curve, determined by plotting the concentration versus the normalized difference in R_{th}, is given in Figure 7. To

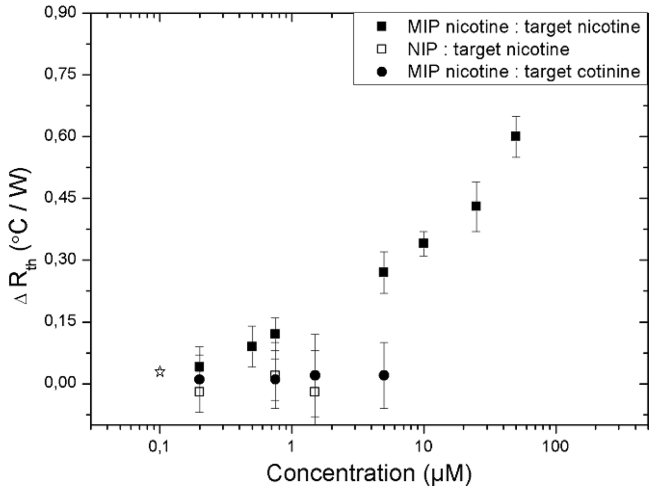

Figure 7. Dose–response curve for the MIP (■), NIP (□), and MIP with cotinine (●), where ΔR_{th} is plotted versus the logarithm of the target concentration. The target concentration of L-nicotine and cotinine varies from 0 to 100 μM in PBS (pH 7.4). The asterisk corresponds to the limit of detection, below this concentration there is no significant response of the MIP to L-nicotine. Adapted with permission from ref 42. Copyright 2014 Springer.

determine the specificity and selectivity of the MIP toward its template, two references were employed. The first is the nonimprinted polymer (NIP) is synthesized in the same manner as the MIP but without the presence of the template and therefore does not contain tailored nanocavities. Another reference is the use of a competitor molecule, in the case of L-nicotine, cotinine was selected (Figure 7).

Figure 7 shows that we can measure in a wide concentration regime, from 0.2 μM (ΔR_{th} = 0.07 ± 0.01 °C/W) to 50 μM (ΔR_{th} = 0.60 ± 0.03 °C/W). With this data, the limit of detection was calculated to be ~100 nM. The sensing platform was also determined to be specific, since the NIP with L-nicotine and the MIP with cotinine did not show a significant response in R_{th}. This demonstrated the proof-of-concept, however the sensor performance can be optimized by reducing the noise level and thereby lower the limit of detection. Geerets et al. determined that the noise on the signal foremost originates from the power supply, which can be controlled by varying the PID parameters.[59] The optimal configuration was found and the detection limit of L-nicotine in buffer solutions improved significantly from 100 nM to 35 nM. Subsequently, this concept was extended to other possible target molecules and additional measurements were performed with MIPs for histamine and serotonin. The results for buffer solutions and the relevant biological concentrations of the target molecules are summarized in Table 1.[42,59] As a first proof-of-application, an experiment was performed with saliva samples spiked with L-nicotine, showing the possibility to use HTM in biological samples.

This proves that the sensor platform is generic; however, it would be more interesting to detect these target molecules simultaneously by employing an array format. Therefore, a novel flow-through sensor cell was developed that is segmented into four quadrants of 2.5 μL each, allowing four parallel measurements to be performed on a single substrate.[60,61] This also enables to correct for nonspecific binding since one of the channels can be functionalized with a NIP. The design is shown in Figure 8.

Table 1. LOD in 1× PBS with HTM Compared to the Biologically Relevant Concentration[a]

	LOD HTM			
target	PBS	saliva	urine	blood
L-nicotine	100 nm	0.2−1000 μm	0.3−10 μm	
serotonin	20 nm			10−1500 nm
histamine	30 nm		200−750 nm	10−1500 nm

[a]Adapted with permission from ref 42. Copyright 2014 Springer.

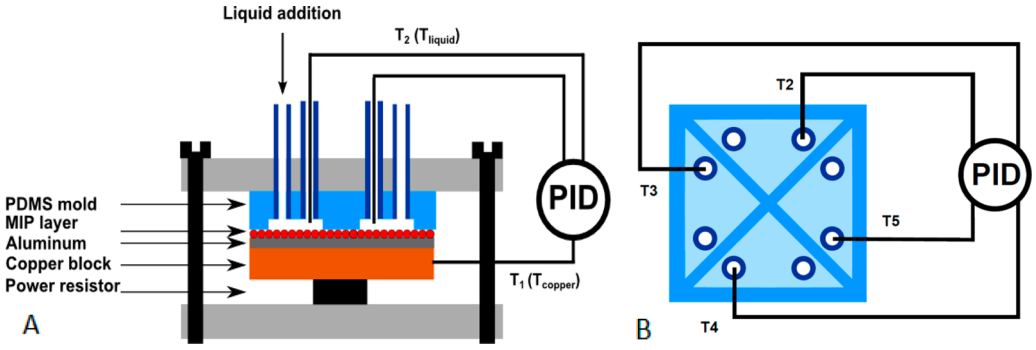

Figure 8. Schematic side (a) and top view (b) of the PDMS flow cell and thermocouples. The PDMS stamp is 10 mm wide and long and has a height of 4 mm. The chambers inside the stamp have a surface area of 5 mm^2 and a height of 0.5 mm. Adapted with permission from ref 60. Copyright 2014 Multidisciplinary Digital Publishing Institute.

To proof the array format capabilities of the novel sensor setup, two experiments with MIPs for different targets were performed. The first was done with a sensor of 50/50 ratio for histamine serotonin, while the second consisted on an equivalent combination of histamine and L-nicotine (Figure 9).

Even though the targets are chemically similar, the sensors only showed a significant response to their corresponding target (Figure 9). This indicates that there is no significant cross-selectivity and the sensor cell can be used in an array format.[60] With the same design, novel MIPs were evaluated that consisted of nanolayers of polymer (∼2 nm) grown onto graphene oxide (GO),[61] which, with its small dimension and high surface-to-volume ratio, can enhance the binding capacity and sensitivity of MIPs. First tests indicate that for histamine detection limits in the same order (∼25 nM) can be achieved as for the conventional bulk MIPs, but by optimizing the sample preparation this can easily be improved. Therefore, this method proves to be a viable alternative, with the benefit that the structure allows miniaturization and the imprint structure can be controlled.

In buffer solutions detection limits of organic molecules can be achieved within the physiologically relevant regime. Additionally, a first proof-of-application with a biological sample, spiked saliva, has been provided. Furthermore, an advanced flow cell design was developed which requires only a very small sample volume (2.5 μL) and can measure in an array format. Besides the more traditional bulk MIPs, a novel MIP-GO hybrid system was presented which has a small dimension (several nanometers) and has to potential to lower the detection limit even further. Summarizing, the HTM approach has proven to be a fast, straightforward and low-cost detection for small organic molecules with MIP-type receptors.

3.4. Detection of Phase Transitions on Supported Lipid Vesicle Layers. An additional HTM-based application is the detection of phase transitions of model lipid membranes, whose study has been mostly carried out for vesicle dispersions in bulk. The aim was to assess whether HTM could detect phase transitions by measuring R_{th} across a lipid vesicle layer deposited onto a hydrogenated NCD film, in contact with a liquid environment. The analysis of thermal transport across a lipid bilayer was so far restricted to molecular simulation studies.[56] The canonical lipid dipalmitoylphosphatidylcholine (DPPC) was selected for this study, the use of which is widespread in the study of phase transitions because of its rich phase behavior in an experimentally accessible temperature range. Within an aqueous environment, the complete melting of the alkyl chains or "main phase transition" takes place at $T \approx 41$ °C.[43,62,63] An advantage of using HTM is that it enables the characterization of solid supported lipid layers without the need of fluorescent labels which may modify the structural properties and, as a consequence, the phase transition behavior of the layer.

Small unilamellar vesicles (SUVs) were formed by power sonication of a DPPC vesicle dispersion in *N*-(2-hydroxyethyl)-piperazine-*N*′-ethanesulfonic acid (Hepes) buffer. Centrifugation was carried out to remove the metallic debris that may have detached from the sonication tip. Dynamic light scattering indicated that vesicles with a mean size of 80 nm were obtained with a polydispersity of 0.2.[43] The substrate onto which vesicle dispersions were deposited was a silicon chip (10 × 10 mm^2, (100) crystalline orientation) covered with a thin layer (∼120 nm, average grain size ∼40 nm) of NCD as shown in Figure 10.

A first control experiment on the blank NCD substrate mounted on copper and exposed to Hepes buffer was performed by applying a heating and cooling scan increasing T_1 from 25 to 60 °C and then cooled to 25 °C at a constant rate of 0.2 °C/min. R_{th} displayed a regular behavior over all the working temperature range (see Figure 11a). Next, an SUV suspension was introduced at 25 °C, a temperature below the observed main phase transition, at a rate of 0.25 mL/min during 5 min. The DPPC vesicle solution was incubated at 25 °C for 1 h and subsequently heated up to 60 °C at a rate of 0.2 °C/min. Once at 60 °C, Hepes buffer was flushed at 50 μL/min for 5 min to remove weakly or nonadsorbed vesicles.

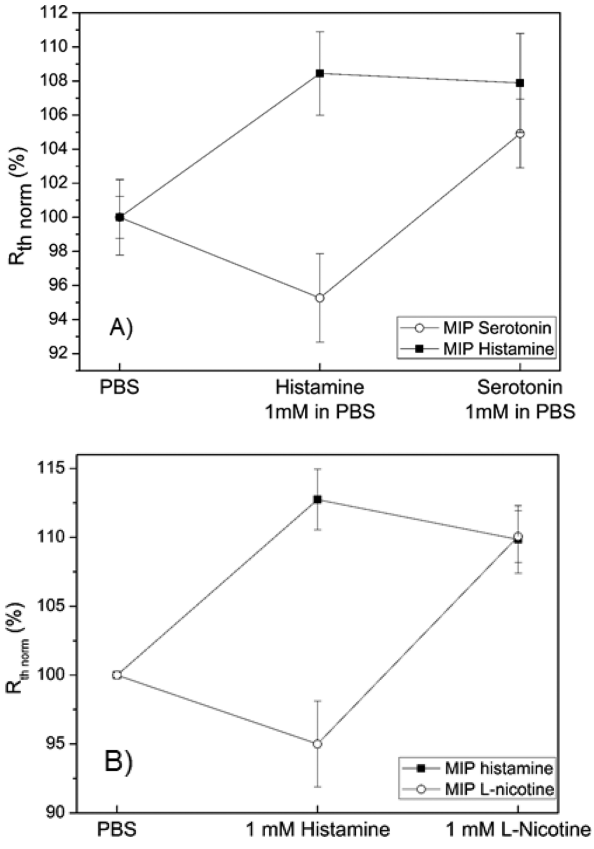

Figure 9. (a) The four quadrants of the flow cell were functionalized with MIP for serotonin and MIP for histamine (50/50%). Upon exposure to a 1 mM solution of serotonin in PBS, the corresponding MIP of serotonin increased significantly, while for the MIP of histamine the signal was slightly lowered. Subsequently, when adding 1 mM histamine in PBS, the MIP for serotonin showed no significant response, while the MIP for histamine increases significantly. (b) The same process was applied as in A, but now the quadrants were functionalized with MIPs for histamine and L-nicotine (50/50%). Again, it can be observed that the MIPs only respond when its corresponding template molecule is applied, showing the possible array formatting of HTM without significant cross selectivity. Adapted with permission from ref 60. Copyright 2014 Multidisciplinary Digital Publishing Institute.

Consecutive alternating cooling and heating runs at 0.2 and 0.3 °C/min were performed following the sequence cooling at 0.2 °C/min, heating at 0.3 °C/min, cooling at 0.3 °C/min, and a last heating at 0.2 °C/min. The complete experiment is illustrated in Figure 11b, which shows raw (nonfiltered) R_{th} data. Noteworthy, reversible anomalies upon heating and cooling can be observed in the temperature of the fluid T_2 and are reflected as jumps in R_{th}. In fact, the temperature at which the jumps are encountered is $T_1 \approx 41$ °C (the temperature of the adsorbed vesicles being essentially that of copper) compare well to the main phase transition temperature observed by other experimental techniques for vesicles in dispersion[43,62,63] indicating that the changes in R_{th} are correlated to the melting phase change.

Interestingly, the size of the jump in R_{th} upon heating and cooling is the same ~0.75 °C/W, thus confirming the reversibility of the effect. Comparing the transition temperature values from heating and cooling hysteresis is observed (see Figure 12a), a characteristic feature of first-order transitions.[64] Certainly at a qualitative level, the observed effective difference R_{th}* in Figure 12b between the two phases (subtracting the contribution of the blank substrate exposed to Hepes buffer from the R_{th} response obtained with DPPC vesicle layer) agrees with the physical picture by molecular dynamics simulations, provided the main contribution of the heat conduction takes places normal to the surface across the adsorbed vesicles.[56] The orientational order of chain molecules promotes an enhancement of the thermal conductivity (thus a decrease of the thermal resistance). The thermal resistance should be lower in the gel phase than in the liquid disordered phase. R_{th} effectively increases upon the phase conversion from gel to liquid disordered, where the alkyl chains of lipid molecules have lost orientational order and gained lateral mobility. On the other hand, a calorimetric effect associated with the observed reversible jumps and reflecting the first order of the transition in R_{th} cannot be ruled out. The transition from the gel to the liquid disordered phase (upon heating) is endothermic: heat is absorbed and the temperature of the surroundings decreases and the thermal resistance increases.

These are the very first measurements of the thermal resistance across a lipid vesicle layer and illustrate the capability of HTM to detect a clear signature of the main phase transition in DPPC at the same temperature as the one obtained by calorimetry,[43,62,63] including its hysteretic behavior. The obtained results can be taken as a starting point for further investigations on more complex lipid mixtures to monitor the formation of lipid rafts,[65] as well as for the use of chemically modified substrates to support other geometries relevant as biosensors platforms such as lipid bilayers and self-assembled monolayers.

4. CONCLUSIONS AND OUTLOOK

In this Spotlight on Applications, a primer into HTM is provided, demonstrating the applicability of the device as a versatile readout technology for biosensor purposes. Promising sensor platforms have been developed by combining HTM with various functional interfaces for the detection of SNPs, human cells, small organic molecules, and phase transitions in lipid vesicle layers. Future research will be oriented toward further improvement of the sensitivity of the readout technology and a deeper incorporation into the field. An

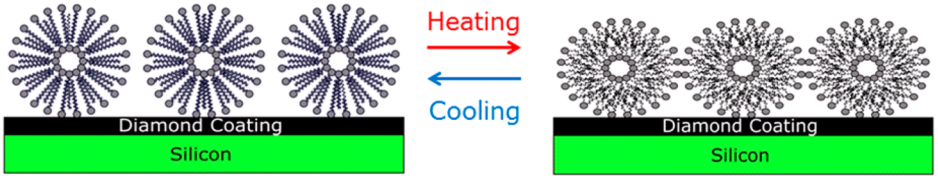

Figure 10. Schematic representation of a layer of DPPC SUVs applied onto a silicon chip covered with hydrogenated NCD. Phase transitions are induced in the lipid vesicle layer by heating and cooling of the substrate, changing the thermal resistance at the solid–liquid interface.

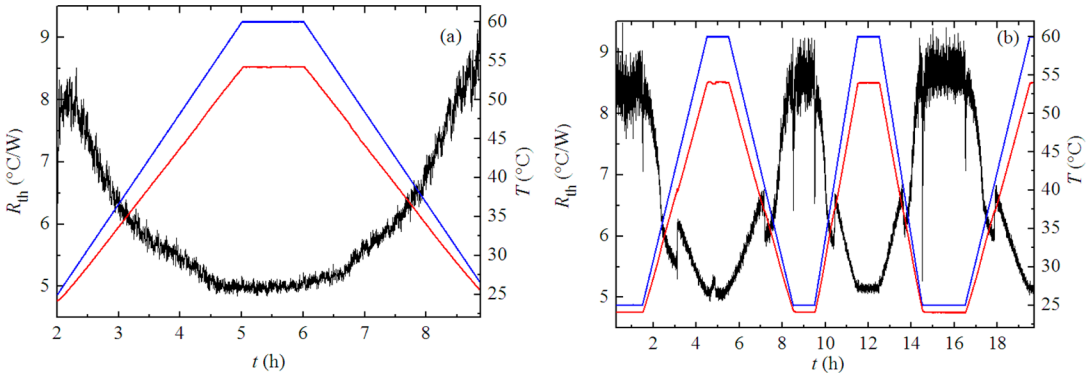

Figure 11. (a) Heating and cooling scans with the substrate exposed to Hepes buffer only: red solid line T_2, blue solid line T_1, black solid line R_{th}. (b) Overview of the experiment after insertion of the DPPC vesicle suspension: black solid line R_{th}, blue solid line T_1, red solid line T_2. Adapted with permission from ref 43. Copyright 2014 Wiley-VCH Verlag GmbH & Co. KGaA.

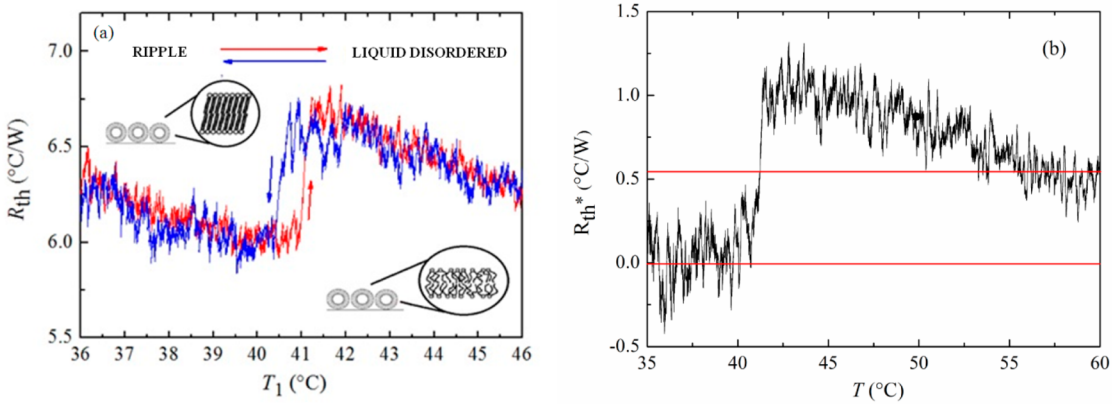

Figure 12. (a) Temperature profile of the heat transfer resistance R_{th} during the main phase transition of a DPPC supported vesicle layer adsorbed on a NCD. The arrows indicate the sense of the run: heating (red solid line) and cooling (blue solid line). (b) Effective R_{th}* = R_{th} (DPPC + Hepes buffer) − R_{th} (Hepes buffer) vs. temperature. Solid red lines: plateaus of R_{th}* values at temperatures away from the main phase transition. Adapted with permission from ref 43. Copyright 2014 Wiley-VCH Verlag GmbH & Co. KGaA.

interesting advantage of this technique is the possibility to detect electrically insulating analytes such as thiols in nonconducting media such as alcohols or oils. Additionally, preliminary results have already been obtained for the detection of the peanut allergen Ara h1 by functionalizing an HTM interface with aptamers. This finding opens the door for the development of a biosensor platform for people suffering from peanut allergy, the most common cause of fatal food-related anaphylaxis.[66] Generally speaking, it can be concluded that HTM can develop into a promising tool for point-of-care diagnostics, a field that is marked by the constant development of new, low-cost devices.[67−69]

AUTHOR INFORMATION

Corresponding Author

*E-mail: bart.vangrinsven@maastrichtuniversity.nl. Phone: +31-43-388.5190. Fax: +31-43-3888.3570.

Present Address

[⊥]Dr. Bart van Grinsven, Maastricht University, Maastricht Science Programme, P.O. Box 616, 6200 MD Maastricht, The Netherlands.

Author Contributions

B.v.G. and K.E. contributed equally to this work. B.v.G. wrote and edited the manuscript in cooperation with K.E., M.P., P.L.P., and P.W. B.v.G. contributed the application regarding SNP detection in DNA. K.E. was responsible for the chapter regarding cell detection. M.P. wrote the part concerning small organic molecule detection by MIPs, and P.L.P. contributed the chapter on phase transition detection in lipid vesicle layers. T.V. designed and drew the schematic figures of the manuscript. P.W. and T.J.C. were responsible for general editing of the manuscript.

Notes

The authors declare no competing financial interest.

ACKNOWLEDGMENTS

This work was financed by the Life Science Initiative of the Province of Limburg, by the Special Research Funds BOF of Hasselt University, the Research Foundation Flanders FWO (Projects G.0B.6213.N and "Methusalem Nano"), and by the Interreg IV-A Project MicroBioMed (European Funds for Regional Development). The authors would also like to thank Dr. H. Dilien and Prof. Dr. W. De Ceuninck for their scientific discussion that helped to improve the quality of the manuscript.

REFERENCES

(1) Turner, A. P. Biosensors: Sense and Sensibility. *Chem. Soc. Rev.* **2013**, *42*, 3184−3196.

(2) Turner, A.; Wilson, G.; Karube, I. *Biosensors: Fundamentals and Applications,* 1st ed.; Oxford University Press: Oxford, U.K., 1987.

(3) Schöning, M. J.; Poghossian, A. Bio FEDS (Field-Effect Devices): State-of-the-Art and New Directions. *Electroanalysis* **2006**, *18* (19−20), 1893−1900.
(4) Vermeeren, V.; Bijnens, N.; Wenmackers, S.; Daenen, M.; Haenen, K.; Williams, O. A.; Ameloot, M.; vandeVen, M.; Wagner, P.; Michiels, L. Towards a Real-Time, Label-Free Diamond-Based DNA Sensor. *Langmuir* **2007**, *23*, 13193−13202.
(5) van Grinsven, B.; Vanden Bon, N.; Grieten, L.; Murib, M. S.; Janssens, S. D.; Haenen, K.; Schneider, E.; Ingebrandt, S.; Schöning, M. J.; Vermeeren, V.; Ameloot, M.; Michiels, L.; Thoelen, R.; De Ceuninck, W.; Wagner, P. Rapid Assessment of the Stability of DNA Duplexes by Impedimetric Real-Time Monitoring of Chemically Induced Denaturation. *Lab Chip* **2011**, *11*, 1656−1663.
(6) Ferreira, M.; Fiorito, P. A.; Oliveira, O. O. J.; Cordoba de Torresi, S. I. Enzyme-Mediated Amperometric Biosensors Prepared with the Layer-by-Layer (LbL) Adsorption Technique. *Biosens. Bioelectron.* **2004**, *19*, 1611−1615.
(7) Llopis, X.; Pumera, M.; Alegret, S.; Merkoçi, A. Lab-on-a-Chip for Ultrasensitive Detection of Carbofuran by Enzymatic Inhibition with Replacement of Enzyme Using Magnetic Beads. *Lab Chip* **2009**, *9*, 213−218.
(8) Yang, J.; Deng, S.; Lei, J.; Ju, H.; Gunasekaran, S. Electrochemical Synthesis of Reduced Graphene Sheet-AuPd Alloy Nanoparticle Composites for Enzymatic Biosensing. *Biosens. Bioelectron.* **2011**, *29*, 159−166.
(9) Held, M.; Schumann, W.; Jahreis, K.; Schmidt, H. L. Microbial Biosensor Array with Transport Mutants of *Escherichia coli* K-12 for the Simultaneous Determination of Mono- and Disaccharides. *Biosens. Bioelectron.* **2002**, *17*, 1089−1094.
(10) Bohrn, U.; Stütz, E.; Fuchs, K.; Fleischer, M.; Schöning, M. J.; Wagner, P. Monitoring of Irritant Gas Using a Whole-Cell-Based Sensor System. *Sens. Actuators, B* **2012**, *175*, 208−217.
(11) Bohrn, U.; Stütz, E.; Fleischer, M.; Schöning, M. J.; Wagner, P. Using a Cell-Based Gas Biosensor for Investigation of Adverse Effects of Acetone Vapors *In Vitro*. *Biosens. Bioelectron.* **2013**, *40*, 393−400.
(12) Cooreman, P.; Thoelen, R.; Manca, J.; vandeVen, M.; Vermeeren, V.; Michiels, L.; Ameloot, M.; Wagner, P. Impedimetric Immunosensors Based on the Conjugated Polymer PPV. *Biosens. Bioelectron.* **2005**, *20*, 2151−2156.
(13) Vermeeren, V.; Grieten, L.; Vanden Bon, N.; Bijnens, N.; Wenmackers, S.; Janssens, S. D.; Haenen, K.; Wagner, P.; Michiels, L. Impedimetric, Diamond-Based Immunosensor for the Detection of C-Reactive Protein. *Sens. Actuators, B* **2011**, *157*, 130−138.
(14) Yano, K.; Karube, I. Molecularly Imprinted Polymers for Biosensor Applications. *Trends Anal. Chem.* **1999**, *18*, 199−204.
(15) Vlatakis, G.; Andersson, L. I.; Müller, R.; Mosbach, K. Drug Assay Using Antibody Mimics Made by Molecular Imprinting. *Nature* **1993**, *361*, 645−647.
(16) Haupt, K.; Mosbach, K. Molecularly Imprinted Polymers and Their Use in Biomimetic Sensors. *Chem. Rev.* **2000**, *100*, 2495−2504.
(17) Piletsky, S. A.; Turner, A. P. F. Electrochemical Sensors Based on Molecularly Imprinted Polymers. *Electroanal.* **2002**, *13*, 317−323.
(18) Hayden, O.; Dickert, F. L. Selective Microorganism Detection with Cell Surface Imprinted Polymers. *Adv. Mater.* **2001**, *13*, 1480−1483.
(19) David, S.; Polonschii, C.; Gheorghiu, M.; Bratu, D.; Dobre, A.; Gheorghiu, E. Assessment of Pathogenic Bacteria Using Periodic Actuation. *Lab Chip* **2013**, *13*, 3192−3198.
(20) Peeters, M.; Troost, F. J.; Mingels, R. H. G.; Welsch, T.; van Grinsven, B.; Vrancken, T.; Ingebrandt, S.; Thoelen, R.; Cleij, T. J.; Wagner, P. M. Impedimetric Detection of Histamine in Bowel Fluids Using Synthetic Receptors with pH-Optimized Binding Characteristics. *Anal. Chem.* **2013**, *85*, 1475−83.
(21) Krajewska, A.; Radecki, J.; Radecka, H. A Voltammetric Biosensor Based on Glassy Carbon Electrodes Modified with Single-Walled Carbon Nanotubes/Hemoglobin for Detection of Acrylamide in Water Extracts from Potato Crisps. *Sensors* **2008**, *8*, 5832−5844.
(22) Norzoui, P.; Ganjali, H.; Larijani, B.; Ganjali, M. R.; Faridbod, F.; Zamani, H. A. A Glucose Biosensor Based on Nanographene and ZnO Nanoparticles Using FFT Continuous Cyclic Voltammetry. *Int. J. Electrochem. Sci.* **2011**, *6*, 5189−5199.
(23) Mao, S.; Yu, K.; Chang, J.; Steeber, D. A.; Ocola, L. E.; Chen, J. Direct Growth of Vertically-Oriented Graphene for Field-Effect Transistor Biosensor. *Sci. Rep.* **2013**, *3*, 1696.
(24) Huck, C.; Poghossian, A.; Bäcker, M.; Chaudhuri, S.; Zander, W.; Schubert, J.; Begoyan, V. K.; Buniatyan, V. V.; Wagner, P.; Schöning, M. J. Capacitively Coupled Electrolyte-Conductivity Sensor Based on High-k Material of Barium Strontium Titanate. *Sens. Actuators, B* **2014**, *198*, 102−109.
(25) Kitade, T.; Kitamura, K.; Konishi, T.; Takegami, S.; Okuno, T.; Ishikawa, M.; Wakabavashi, M.; Nishikawa, K.; Muramatsu, Y. Potentiometric Immunosensor Using Artificial Antibody Based on Molecularly Imprinted Polymers. *Anal. Chem.* **2004**, *76*, 6802−6807.
(26) D'Agostino, G.; Alberti, G.; Biesuz, R.; Pesavento, M. Potentiometric Sensor for Atrazine Based on a Molecular Imprinted Membrane. *Biosens. Bioelectron.* **2006**, *22*, 145−152.
(27) Marzouk, S. A.; Ashraf, S. S.; Tayyari, K. A. Prototype Amperometric Biosensor for Sialic Acid Determination. *Anal. Chem.* **2007**, *79*, 1668−1674.
(28) Ohnuki, H.; Saiki, T.; Kusakari, A.; Endo, H.; Ichihara, M.; Izumi, M. Incorporation of Glucose Oxidase into Langmuir-Blodgett Films Based on Prussian Blue Applied to Amperometric Glucose Biosensor. *Langmuir* **2007**, *23*, 4675−4681.
(29) Feng, S.; Gao, F.; Che, Z.; Grant, E.; Kitts, D. D.; Wang, S.; Lu, X. Determination of α-Tocopherol in Vegetable Oils Using a Molecularly Imprinted Polymers-Surface-Enhanced Raman Spectroscopic Biosensor. *J. Agric. Food Chem.* **2013**, *61*, 10467−10475.
(30) Merkl, S.; Vornicescu, D.; Dassinger, N.; Keusgen, M. Detection of Whole Cells Using Reflectometric Interference Spectroscopy. *Phys. Status Solidi* **2014**, *211*, 1416−1422.
(31) Feng, L.; Liu, Y.; Hu, J. Molecularly Imprinted TiO_2 Thin Film by Liquid Phase Deposition for the Determination of L-Glutamic Acid. *Langmuir* **2004**, *20*, 1786−1790.
(32) Fei, Y. H.; Liu, D.; Wu, Z. S.; Shin, G. L.; Yu, R. Q. DNA-Encoded Signal Conversion for Sensitive Microgravimetric Detection of Small Molecule-Protein Interaction. *Bioconjugate Chem.* **2011**, *22*, 2369−2376.
(33) Reyes-Romero, D. F.; Behrmann, O.; Dame, G.; Urban, G. A. Dynamic Thermal Sensor for Biofilm Monitoring. *Sens. Actuators, A* **2014**, *213*, 43−51.
(34) Sauerbrey, G. Verwendung von Schwingquarzen zur Wägung Dünner Schichten und zur Mikrowägung. *Z. Phys.* **1959**, *155*, 206−222.
(35) Berggren, C.; Johansson, G. Capacitance Measurements of Antibody-Antigen Interactions in a Flow System. *Anal. Chem.* **1997**, *69*, 3651−3657.
(36) Wade, R. C.; Gabdoulline, R. R.; Lüdemann, S. K.; Lounnas, V. Electrostatic Steering and Ionic Tethering in Enzyme-Ligand Binding: Insights from Simulations. *Proc. Natl. Acad. Sci. U.S.A.* **1998**, *95*, 5942−5949.
(37) Panasyuk, T. L.; Mirsky, V. M.; Piletsky, S. A.; Wolfbeis, O. S. Electropolymerized Molecularly Imprinted Polymers as Receptor Layers in Capacitive Chemical Sensors. *Anal. Chem.* **1999**, *71*, 4609.
(38) Dekker, C.; Ratner, M. Electronic Properties of DNA. *Phys. World* **2001**, *14*, 29−33.
(39) Cuniberti, G.; Graco, L.; Porath, D.; Dekker, C. Backbone-Induced Semiconducting Behavior in Short DNA Wires. *Phys. Rev. B* **2002**, *65*, 241314.
(40) van Grinsven, B.; Vanden Bon, N.; Strauven, H.; Grieten, L.; Murib, M. S.; Jimenez Monroy, K. L.; Janssens, S. D.; Haenen, K.; Schöning, M. J.; Vermeeren, V.; Ameloot, M.; Michiels, L.; Thoelen, R.; De Ceuninck, W.; Wagner, P. Heat-transfer resistance at Solid-Liquid Interfaces: A Tool for the Detection of Single-Nucleotide Polymorphisms in DNA. *ACS Nano* **2012**, *6*, 2712−2721.
(41) Eersels, K.; van Grinsven, B.; Ethirajan, A.; Timmermans, S.; Jiménez Monroy, K. L.; Bogier, J. F. J.; Punniyakoti, S.; Vandenryt, T.; Hendriks, J. J. A.; Cleij, T. J.; Daemen, M. J. A. P.; Somers, V.; De Ceuninck, W.; Wagner, P. Selective Identification of Macrophages and

Cancer Cells Based on Thermal Transport through Surface-Imprinted Polymer Layers. *ACS Appl. Mater. Interfaces* **2013**, *5*, 7258−7267.
(42) Peeters, M.; Csipai, P.; Geerets, B.; Weustenraed, A.; van Grinsven, B.; Thoelen, R.; Gruber, J.; De Ceuninck, W.; Cleij, T. J.; Troost, F. J.; Wagner, P. Heat-Transfer-Based Detection of L-Nicotine, Histamine, and Serotonin Using Molecularly Imprinted Polymers as Biomimetic Receptors. *Anal. Bioanal. Chem.* **2013**, *405*, 6453−6460.
(43) Losada-Pérez, P.; Jiménez-Monroy, K. L.; van Grinsven, B.; Leys, J.; Janssens, S. D.; Peeters, M.; Glorieux, C.; Thoen, J.; Haenen, K.; De Ceuninck, W.; Wagner, P. Phase Transitions in Lipid Vesicles Detected by a Complementary Set of Methods: Heat-Transfer Measurements, Adiabatic Scanning Calorimetry and Dissipation-Mode Quartz Crystal Microbalance. *Phys. Status Solidi A* **2014**, *211*, 1377−1388.
(44) Kodama, T.; Jain, A.; Goodson, K. E. Heat Conduction Through a DNA-Gold Composite. *Nano Lett.* **2009**, *9*, 2005−2009.
(45) Janssens, S. D.; Pobedinskas, P.; Vacik, J.; Petráková, V.; Ruttens, B.; D'Haen, J.; Nesládek, M.; Haenen, K.; Wagner, P. Separation of Intra- and Intergranular Magnetotransport Properties in Nanocrystalline Diamond Films on the Metallic Side of the Metal-Insulator Transition. *New J. Phys.* **2011**, *13*, 083008.
(46) Christiaens, P.; Vermeeren, V.; Wenmackers, S.; Daenen, M.; Haenen, K.; Nesládek, M.; vandeVen, M.; Ameloot, M.; Michiels, L.; Wagner, P. EDC-Mediated DNA Attachment to Nanocrystalline CVD Diamond Films. *Biosens. Bioelectron.* **2006**, *22*, 170−177.
(47) Vermeeren, V.; Wenmackers, S.; Daenen, M.; Haenen, K.; Williams, O. A.; Ameloot, M.; vandeVen, M.; Wagner, P.; Michiels, L. Topographical and Functional Characterisation of the ssDNA Probe Layer Generated Through EDC-Mediated Covalent Attachment to Nanocrystalline Diamond Using Fluorescence Microscopy. *Langmuir* **2008**, *24*, 9125−9134.
(48) Ambia-Garrido, J.; Vainrub, A.; Pettitt, B. M. A Model for Structure and Thermodynamics of ssDNA and dsDNA Near a Surface: A Coarse Grained Approach. *Comput. Phys. Commun.* **2010**, *181*, 2001−2007.
(49) Wenmackers, S.; Vermeeren, V.; vandeVen, M.; Ameloot, M.; Bijnens, N.; Haenen, K.; Michiels, L.; Wagner, P. Diamond-Based DNA Sensors: Surface Functionalization and Readout Strategies. *Phys. Status Solidi A* **2009**, *206*, 391−408.
(50) Rezek, B.; Shin, D.; Nebel, C. E. Properties of Hybridized DNA Arrays on Single-Crystalline Undoped and Boron-Doped (100) Diamonds Studied by Atomic Force Microscopy in Electrolytes. *Langmuir* **2007**, *23*, 7626−7633.
(51) Wenmackers, S.; Pop, S. D.; Roodenko, K.; Vermeeren, V.; Williams, O. A.; Daenen, M.; Douheret, O.; D'Haen, J.; Hardy, A.; Van Bael, M. K.; Hinrichs, K.; Cobet, C.; vandeVen, M.; Ameloot, M.; Haenen, K.; Michiels, L.; Esser, N.; Wagner, P. Structural and Optical Properties of DNA Layers Covalently Attached to Diamond Surfaces. *Langmuir* **2008**, *24*, 7269−7277.
(52) Bers, K.; van Grinsven, B.; Vandenryt, T.; Murib, M.; Janssen, W.; Geerets, B.; Ameloot, M.; Haenen, K.; Wagner, P. Implementing Heat Transfer Resistivity as a Key Element in a Nanocrystalline Diamond Based Single Nucleotide Polymorphism Detection Array. *Diamond Relat. Mater.* **2013**, *38*, 45−51.
(53) Cornelis, P.; Vandenryt, T.; Wackers, G.; Kellens, E.; Losada-Pérez, P.; Thoelen, R.; De Ceuninck, W.; Eersels, K.; Drijkoningen, S.; Haenen, K.; Peeters, M.; van Grinsven, B.; Wagner, P. Heat Transfer Resistance as a Tool to Quantify Hybdrization Efficiency of DNA on a Nanocrystalline Diamond Surface. *Diamond Relat. Mater.* **2014**, *48*, 32−36.
(54) Vanden Bon, N.; van Grinsven, B.; Murib, M. S.; Siang Yeap, W.; Haenen, K.; De Ceuninck, W.; Wagner, P.; Ameloot, M.; Vermeeren, V.; Michiels, L. Heat-Transfer-Based Detection of SNPs in the PAH Gene of PKU Patients. *Int. J. Nanomed.* **2014**, *9*, 1629−1640.
(55) Alexander, C.; Vulfson, E. V. Spatially Functionalized Polymer Surfaces Produced via Cell-Mediated Lithography. *Adv. Mater.* **1997**, *9*, 751−755.
(56) Nakano, T.; Kikugawa, G.; Ohara, T. A Molecular Dynamics Study on Heat Conduction Characteristics in DPPC Lipid Bilayer. *J. Chem. Phys.* **2010**, *133*, 154705.
(57) Scholtens, T. M.; Schreuder, F.; Ligthart, S. T.; Swennenhuis, J. F.; Greve, J.; Terstappen, L. W. M. M. Automated Identification of Circulating Tumor Cells by Image Cytometry. *Cytometry, Part A* **2012**, *81A*, 138−148.
(58) Bers, K.; Eersels, K.; van Grinsven, B.; Daemen, M.; Bogie, J. F.; Hendriks, J. J.; Bouwmans, E. E.; Püttmann, C.; Stein, C.; Barth, S.; Bos, G. M.; Germeraad, W. T.; De Ceuninck, W.; Wagner, P. Heat-Transfer Resistance Measurement Method (HTM)-Based Cell Detection at Trace Levels using a Progressive Enrichment Approach with Highly Selective Cell-Binding Surface Imprints. *Langmuir* **2014**, *30*, 3631−3639.
(59) Geerets, B.; Peeters, M.; van Grinsven, B.; Bers, K.; De Ceuninck, W.; Wagner, P. Optimizing the Thermal Readout Technique for MIP-Based Biomimetic Sensors: Towards Nanomolar Detecion Limits. *Sensors* **2013**, *13*, 9148−9159.
(60) Wackers, G.; Vandenryt, T.; Cornelis, P.; Kellens, E.; Thoelen, R.; De Ceuninck, W.; Losada Pérez, P.; van Grinsven, B.; Peeters, M.; Wagner, P. Array Formatting of the Heat-Transfer Method (HTM) for the Detection of Small Organic Molecules by Molecularly Imprinted Polymers. *Sensors* **2014**, *14*, 11016−11030.
(61) Peeters, M.; Kobben, S.; Jiménez-Monroy, K.; Modesto, L.; Kraus, M.; Vandenryt, T.; Gaulke, A.; van Grinsven, B.; Ingebrandt, S.; Junkers, T.; Wagner, P. Thermal Detection of Histamine with a Graphene Oxide Based Molecularly Imprinted Polymer Platform Prepared by Reversible Addition-Fragmentation Chain Transfer Polymerization. *Sens. Actuators, B* **2014**, *203*, 527−535.
(62) Privalov, P. L. Scanning Microcalorimeters for Studying Macromolecules. *Pure Appl. Chem.* **1980**, *52*, 479−497.
(63) Mabrey, S.; Sturtevant, J. M. Investigation of Phase Transitions of Lipids and Lipid Mixtures by High Sensitivity Differential Scanning Calorimetry. *Proc. Natl. Acad. Sci. U.S.A.* **1976**, *73*, 3862−3866.
(64) Zammit, U.; Marinelli, M.; Mercuri, F.; Paoloni, S. Analysis of the Order Character of the R(II)-R(I) and the R(I)-R(V) Rotator Phase Transitions in Alkanes by Photopyroelectric Calorimetry. *J. Phys. Chem. B* **2010**, *114*, 8134−8139.
(65) Simons, K.; Ikonen, E. Functional Rafts in Cell Membranes. *Nature* **1997**, *387*, 569−572.
(66) Sicherer, S. H.; Sampson, H. A. Food Allergy. *J. Allergy Clin. Immunol.* **2006**, *117*, 470−475.
(67) Gupta, R.; Reifenberger, R. G.; Kulkarni, G. U. Cellphone Camera Imaging of a Periodically Patterned Chip as a Potential Method for Point-of-Care Diagnostics. *ACS Appl. Mater. Interfaces* **2014**, *6*, 3923−3929.
(68) Sun, D.; Guo, T.; Ran, Y.; Huang, Y.; Guan, B. O. *In Situ* DNA Hybridization Detection with a Reflective Microfiber Grating Biosensor. *Biosens. Bioelectron.* **2014**, *61*, 541−546.
(69) Lehr, J.; Fernanders, F. C. B.; Bueno, P. R.; Davis, J. J. Label-free Capacitive Diagnostics: Exploiting Local Redox Probe State Occupancy. *Anal. Chem.* **2014**, *86*, 2559−2564.

NOTE ADDED AFTER ASAP PUBLICATION

This paper was published on the Web on August 14, 2014, with the author Thomas J. Cleij's name misspelled, along with a minor error in the Abstract graphic. The corrected version was reposted on August 18, 2014.